IEEE Access
Multidisciplinary | Rapid Review | Open Access Journal

Date of publication xxxx 00, 0000, date of current version xxxx 00, 0000.

Digital Object Identifier 10.1109/ACCESS.2017.Doi Number

A Multimodal Neural Activity Readout Integrated Circuit for Recording Fluorescence and Electrical Signals

TAEJU LEE[1], (Member, IEEE), JEE-HO PARK[2], (Student Member, IEEE), NAMSUN CHOU[3], (Member, IEEE), IL-JOO CHO[3], (Member, IEEE), SEONG-JIN KIM[2], (Member, IEEE), and MINKYU JE[1], (Senior Member, IEEE)

[1]School of Electrical Engineering, Korea Advanced Institute of Science and Technology (KAIST), Daejeon 34141, Republic of Korea
[2]School of Electrical and Computer Engineering, Ulsan National Institute of Science and Technology (UNIST), Ulsan 44919, Republic of Korea
[3]Center for BioMicrosystems, Brain Science Institute, Korea Institute of Science and Technology (KIST), Seoul 02792, Republic of Korea

E-mail: taeju.lee@kaist.ac.kr, mkje@kaist.ac.kr

This work was supported by the Brain Research Program under Grant 2017M3C7A1028859 and the Information Technology Research Center (ITRC) Program under Grant IITP-2020-0-01778 funded by the Ministry of Science and ICT (MSIT), Korea. The chip fabrication and EDA tool were supported by the IC Design Education Center (IDEC), Korea.

ABSTRACT Monitoring the electrical neural signals is an important method for understanding the neuronal mechanism. In particular, in order to perform a cell-type-specific study, it is necessary to observe the concentration of calcium ions using fluorescent indicators in addition to measuring the electrical neural signal. This paper presents a multimodal multichannel neural activity readout integrated circuit that can perform not only electrical neural recording but also fluorescence recording of neural activity for the cell-type-specific study of heterogeneous neuronal cell populations. For monitoring the calcium ions, the photodiode generates the current according to the fluorescence expressed by the reaction between the genetically encoded calcium indicators and calcium ions. The time-based fluorescence recording circuit then records the photodiode current. The electrical neural signal captured by the microelectrode is recorded through the low-noise amplifier, variable gain amplifier, and analog-to-digital converter. The proposed integrated circuit is fabricated in a 1-poly 6-metal (1P6M) 0.18-μm CMOS process. The fluorescence recording circuit achieves a recording range of 81 dB (75 pA to 860 nA) and consumes a power of 724 nW/channel. The electrical recording circuit achieves an input-referred noise of 2.7 μV_{rms} over the bandwidth of 10 kHz, while consuming the power of 4.9 μW/channel. The functionality of the proposed circuits is verified through the *in vivo* and *in vitro* experiments. Compared to the conventional neuroscience tools, which consist of bulky off-chip components, this neural interface is implemented in a compact size to perform multimodal neural recording while consuming low power.

INDEX TERMS Brain-machine interface, heterogeneous cell population, fluorescence recording, calcium ion, genetically encoded calcium indicator, GECI, G-CaMP, R-CaMP, electrical neural recording.

I. INTRODUCTION

The brain is a complex structure made up of tens of billions of neurons and tens of trillions of connections. The brain consists of a heterogeneous cell population that engages in neuronal activity by communicating biological signals between the cells. In an intricate brain neural network, the action potentials (APs) and local field potentials (LFPs) are key components that enable understanding of the intracellular and extracellular neural mechanisms. Furthermore, these electrical signals are used to study neurological and psychiatric disorders, implement neural prosthesis, and perform next-generation neuroscience research.

This article has been accepted for publication in a future issue of this journal, but has not been fully edited. Content may change prior to final publication. Citation information: DOI 10.1109/ACCESS.2021.3107299, IEEE Access

In addition, the recording of APs and LFPs becomes important for conducting research related to the central nervous system (CNS) and peripheral nervous system (PNS). Recently, for the purpose of implementing the brain-computer interface, drug-screening platform, and next-generation neuroscience tool such as a large-scale high-throughput neural recording instrument, multichannel electrical recording systems have been developed to monitor the neural activity [1]–[14]. However, recording solely based on electrical means has inherent limitations as follows:

(1) Susceptibility to electrical disturbances such as powerline interferences and stimulation artifacts
(2) Lack of measuring biologically significant signals induced by chemical elements such as calcium ion, dopamine, glutamate, etc.
(3) Difficulties in biological network analysis due to the above limitations
(4) Lack of signal tracking for the specific type of cell populations

Therefore, the neural recording should be performed in multiple modalities. Prior works [4], [6], [9]–[11], [14] presented multimodal neural recording integrated circuits (ICs), which record neural activities in multiple modalities, but these systems still have limitations to perform the cell-type-specific study in a heterogeneous population of cells.

When the neuronal cells are activated, they not only generate electrical signals but also release neurotransmitters at their synaptic clefts and ions through the channels in their membranes. The systems in [6] and [14] can measure the electrical signals and chemical signals related to neurotransmitters. In particular, by monitoring neurotransmitters along with electrical signals, it is possible to obtain richer information through signal processing compared to when measuring only electrical signals. However, the type of firing cells still cannot be specified.

In addition, in the *in-vitro* platform, multimodal neural interfaces that perform the optical imaging and impedance monitoring functions are presented to characterize the cell morphology and cell attachment, respectively [6], [9]. However, none of these systems provides a cell-type-specific monitoring function.

To enable cell-type-specific study in a heterogeneous population of neuronal cells, we present a multimodal neural activity readout IC with the following two features: 1) a fluorescence recording channel combined with a photodiode for monitoring the Ca^{2+} associated with the neural firing, 2) an electrical recording channel combined with a microelectrode array to acquire APs and LFPs [16]. The simplified system operation, IC performance results, and *in vitro* measurement results were first presented in [16]. In this paper, we present an extended version with

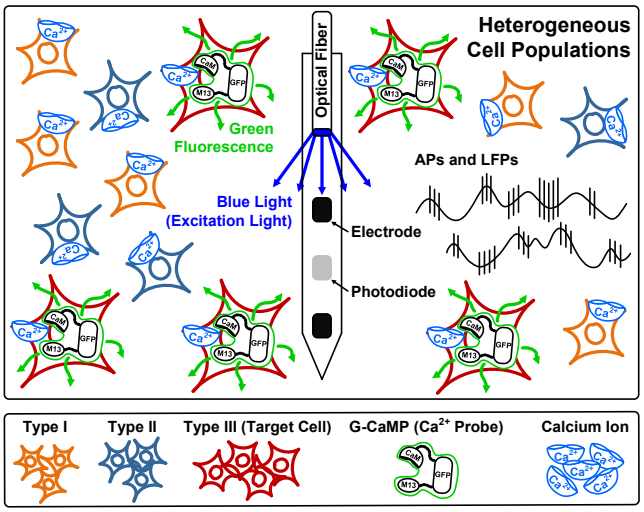

FIGURE 1. Concept of genetically-encoded-calcium-indicator-based fluorescence recording and electrical recording.

content, including a review of prior works, circuit analysis, and animal experiment results.

When the cells produce neural spikes, the calcium ions are also released through the ion channels in their membranes. For monitoring the Ca^{2+} concentration, the genetically encoded calcium indicator (GECI) is used as the Ca^{2+} probe, which emits the fluorescence when it is combined with the Ca^{2+} [17], [18]. At this time, a cell-type-specific monitoring function is possible by measuring the emitted fluorescence through the photodiode. In particular, G-CaMP (emitting green fluorescence) and R-CaMP (emitting red fluorescence) are representative GECIs that are composed of green fluorescent protein (GFP) and red fluorescent protein (RFP), respectively, calcium-modulated protein (CaM), and M13 fragment of myosin light chain kinase [17], [18] as shown in Fig. 1. In this work, we measure the change of the Ca^{2+} concentration using the G-CaMP6f emitting the green fluorescent light.

Fig. 1 shows the concept of GECI-based fluorescence and electrical monitoring functions through the photodiode and microelectrode array, respectively. Before measuring the Ca^{2+}, the excitation light from the optical fiber excites GECIs. These activated GECIs operate as Ca^{2+} probes and emit green (or red) fluorescence when combined with Ca^{2+}. Since the Ca^{2+} probes are genetically encoded to attach to the target cells, it is possible to know which type of cell population is activated when the Ca^{2+} is released according to the firing of the target cells.

When neuronal cells generate electrical signals and release Ca^{2+}, these two kinds of signals have different characteristics. In the active state, cells generate spikes in a time scale of 0.15 ms to 10 ms [19], [20], while the Ca^{2+} is released from their membranes at a slow rate in the time scale of 200 ms to 10 s [21]–[25]. The neuronal mechanism that induces behavior, emotion, sensation, and vision

This article has been accepted for publication in a future issue of this journal, but has not been fully edited. Content may change prior to final publication. Citation information: DOI 10.1109/ACCESS.2021.3107299, IEEE Access

recognition is achieved by signaling between the functional areas such as the prefrontal area, premotor area, primary motor cortex, etc. Each functional area is composed of various types of cell populations. Therefore, in order to understand the neuronal mechanism in these cell populations, fluorescence-marker-based cell-type-specific recording is an important factor.

This paper is organized as follows. The prior works that record electrical signals and neurotransmitters are reviewed in Section II. The details of the fluorescence and electrical recording circuits are described in Section III. The measured chip performance is presented in Section IV. Section V presents the *in vivo* and *in vitro* measurement results and experimental setup. Also, the performances of the implemented chip are summarized and compared with other state-of-the-art works. Finally, Section VI concludes this work.

II. Prior Works

For characterizing the cells *in vivo* and *in vitro*, multimodal neural recording systems have been implemented. Fig. 2 summarizes the three modalities that are widely applied to neural engineering tools. The key modalities can be categorized as follows:

(1) Electrical recording of APs and LFPs
(2) Recording of chemical neurotransmitters such as dopamine, serotonin, glutamate, etc.
(3) Impedance monitoring between the cell and electrode

A. MODALITY 1: ELECTRICAL RECORDING

In neuroscience and neuroprosthetic research, electrical recording is the basic and easily applicable modality. For monitoring APs and LFPs with low noise characteristics while consuming low power, the recording circuit structure consisting of the capacitively-coupled instrumentation amplifier (CCIA) and the successive-approximation-register analog-to-digital converter (SAR ADC) is widely used to implement the neural recording system [2]–[4], [6], [8], [12], [13], as shown in Fig. 2 (a).

The CCIA is used to amplify tiny neural signals with adding a minimal amount of noise so that a good signal-to-noise ratio (SNR) can be obtained. Its capacitively coupled input structure provides an inherent AC-coupling characteristic, allowing the amplifier operation not to be affected by the electrode offset voltage at DC. The following buffer stage drives the sampling capacitance of the ADC with sufficiently low output impedance and driving capability. Out of many different types of ADCs, the SAR ADC is often used for digitizing the recorded neural signals due to its excellent energy efficiency. Due to the high voltage gain provided by the CCIA, a low-resolution ADC such as the SAR ADC can be used to minimize the power consumption while obtaining a sufficient SNR.

However, the recording system employing the high-gain CCIA followed by the SAR ADC has a limitation in achieving a wide dynamic range performance. In other words, if there are external interferences such as stimulation artifacts present in the bidirectional neural interface system, the CCIA can easily fall into saturation or distort the signal significantly due to its high gain. For the applications where dealing with such interferences are essential, the recording circuit structure that employs a low-gain CCIA and a high-resolution ΔΣ ADC is proposed [26]–[28].

B. MODALITY 2: CHEMICAL RECORDING

In addition to measuring electrical signals, the recording of neurotransmitters provides important information for studying neurological phenomena. For example, the depletion of dopamine in the striatum is related to the cause of Parkinson's disease [29]. Serotonin regulates various biological phenomena such as cardiovascular function, bladder control, etc [30]. Fig. 2 (b) presents the circuit topology used for chemical recording [6], [14], [15].

Three electrodes composed of a counter electrode (CE), a reference electrode (RE), and a working electrode (WE) are combined with a transimpedance amplifier (TIA) to measure the current generated by the chemical reaction on the electrode surface. When the CE and WE sustain the voltage difference of V_{CE}–V_{WE}, the chemical reaction occurs on the surface of the WE. The current resulted from the reaction flows through the CE and WE.

Due to the feedback formed by the operation amplifier between the RE and CE, the voltage of CE (V_{CE}) follows the stimulation voltage (V_S). According to the waveform of the applied V_S, the method can be classified into cyclic voltammetry (CV) and constant potential amperometry (CA). The method (CV or CA) is widely used for monitoring neurotransmitters, and the observation of neurotransmitters is an important factor in studying neurological disorders such as Alzheimer's and Parkinson's diseases.

C. MODALITY 3: IMPEDANCE MONITORING

Monitoring the impedance of the electrode-cell interface provides valuable information for understanding the cell structure, cell distribution, and electrode status. Fig. 2 (c) shows the topology of the impedance monitoring circuits [4], [6], [9], [10], [31]. For recording the impedance Z_{EL} between the electrode and the cell, the excitation voltage V_S (or current I_S) is applied between the reference and working electrodes. The resulting current I_S (or voltage V_S) due to the applied V_S (or I_S) flows through the Z_{EL} ($I_S = V_S / Z_{EL}$). Then, the I_S (or V_S) is recorded through the amplifier, buffer, and ADC.

This article has been accepted for publication in a future issue of this journal, but has not been fully edited. Content may change prior to final publication. Citation information: DOI 10.1109/ACCESS.2021.3107299, IEEE Access

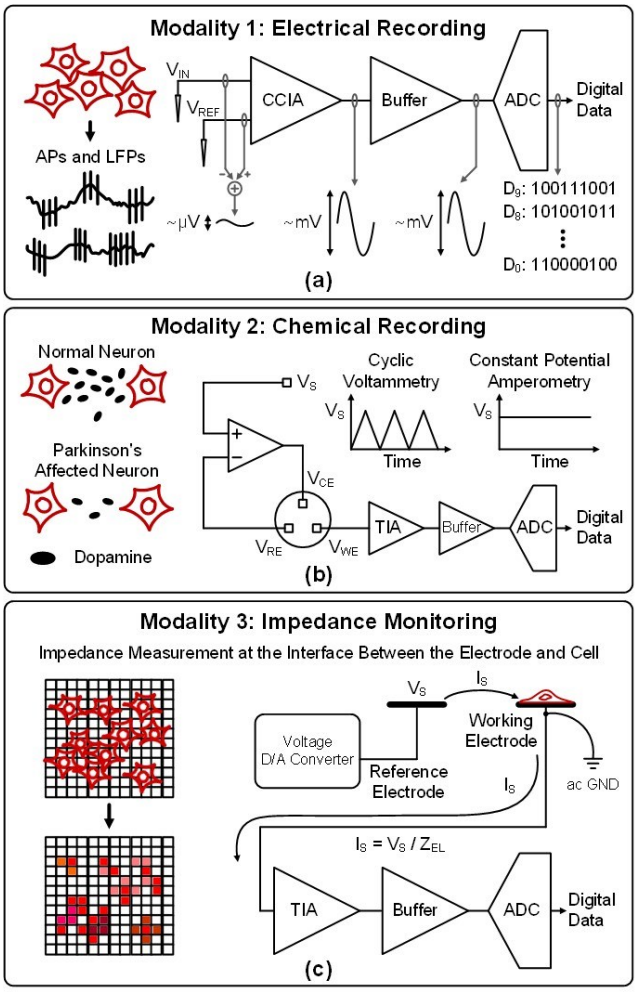

FIGURE 2. Key modalities applied to the prior multimodal neural recording systems.

Based on such an electrode-cell impedance measurement technique, the cell distribution and attachment can be identified in the two-dimensional (2D) *in vitro* platform [4], [9], [10]. Other applications generate the images of individual cell structures by integrating a high-density electrode array and impedance measurement channels [6], [31]. Recently, to overcome the drawbacks of the 2D impedance monitoring system, the three-dimensional (3D) monitoring system was developed [32]. Cell modeling can thus be performed similarly to the *in vivo* environment using the 3D *in vitro* platform. As described above, impedance monitoring is an important neural engineering tool, which is actively used in the field of drug screening and cancer cell study [33], [34].

III. Multimodal Neural Activity Readout IC

A. OVERALL SYSTEM CONCEPT

The proposed multimodal neural activity readout IC is composed of two kinds of front-ends, fluorescence and electrical recording channels. While the electrical recording channel monitors the electrical signals through the electrode array, the fluorescence recording channel records the photodiode current that is induced by green (or red) fluorescence emitted from Ca^{2+} probes when combined with the Ca^{2+}.

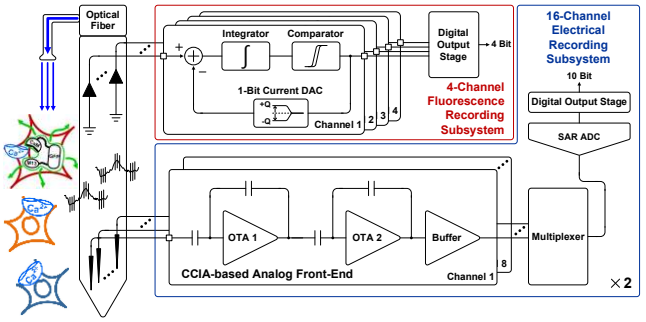

FIGURE 3. Block diagram of the proposed multimodal neural activity readout IC.

When cells are activated, two kinds of front-ends measure the Ca^{2+} concentration and electrical signals. Each of these signals is generated at different rates. The neural spikes are generated at a rate in a time scale of 0.15 ms to 10 ms [19], [20], while the Ca^{2+} is released at a slow rate in a time scale of 200 ms to 10 s [21]–[25]. The electrical recording channel, therefore, should perform fast digitization of the input signals with an energy-efficient operation for use *in vivo*. On the other hand, the fluorescence recording channel can be implemented to perform a slow digital conversion of the photodiode current. In this work, to satisfy the different requirements and maintain low-power operation while retaining the system performance for both fluorescence and electrical recording functions, the time-domain topology is applied to the fluorescence recording channel, and the CCIA-based topology is employed for the electrical recording channel.

Fig. 3 shows a system block diagram of the multimodal neural activity readout IC, which consists of 4 fluorescence recording channels and 16 electrical recording channels. The fluorescent light emitted from the Ca^{2+} probes is measured by the photodiode and fluorescence recording channel. The electrical signal is measured by the electrode array and the electrical recording channel. After the digital conversion of both fluorescence and electrical recording channels, the digital output voltage level is up-shifted from 1 V to 1.8 V, while the rest of the recording circuits are driven by a 1-V supply.

B. FLUORESCENCE RECORDING CIRCUIT

Fig. 4 shows a schematic of the time-based fluorescence recording channel that records the input current I_{IN} generated by the photodiode. For time-based operation, the channel is composed of a current digital-to-analog converter (I-DAC), an operational transconductance amplifier (OTA) A_0, a feedback capacitor C_F, the delay

This article has been accepted for publication in a future issue of this journal, but has not been fully edited. Content may change prior to final publication. Citation information: DOI 10.1109/ACCESS.2021.3107299, IEEE Access

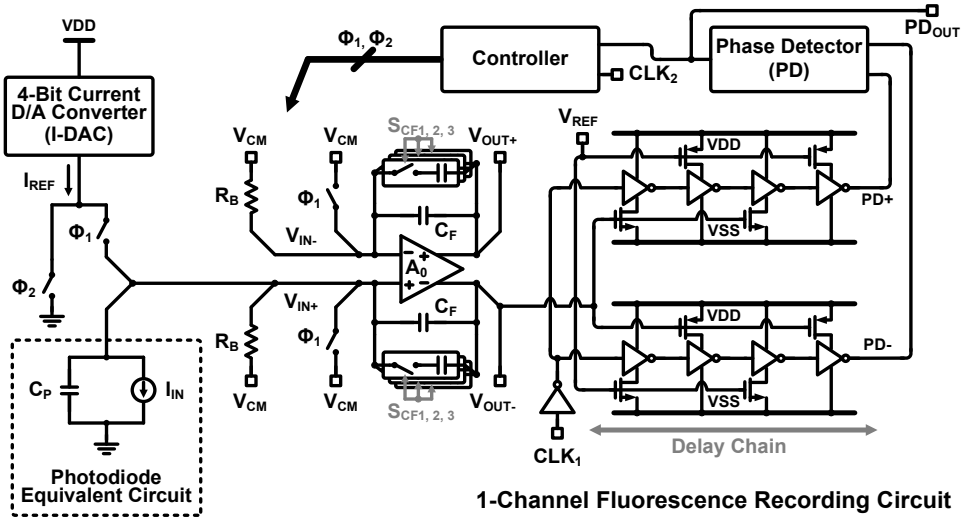

FIGURE 4. Schematic of the time-based fluorescence recording channel.

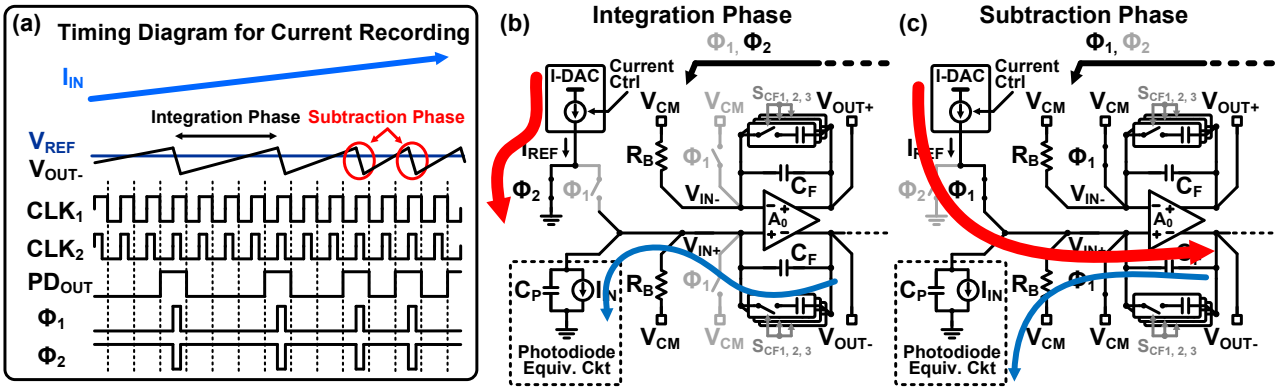

FIGURE 5. (a) Timing diagram of the time-based fluorescence recording channel. (b) Circuit operations in the integration phase, and (c) subtraction phase.

chain presented in [35], a phase detector, and a controller. The digitization of I_{IN} is carried out by iterative operation of the integration and subtraction. To perform integration and subtraction of I_{IN}, the switches of Φ_1 and Φ_2 are controlled by the output signals of the controller. The operating clock CLK_1 is used in the delay chains for converting the voltage difference to the difference of phase delay. CLK_2 is applied to the controller for determining the amount of subtracted current in the subtraction phase. Finally, the phase detector generates the output bit of PD_{OUT} as a result of I_{IN}.

Fig. 5 (a) shows the timing diagram of the time-based operation. First, to record I_{IN} in the integration phase, the Φ_1 is off, and Φ_2 is on (Fig. 5 (b)). When the photodiode detects the fluorescent light, I_{IN} is integrated through C_F. The reference current I_{REF} of the I-DAC flows to the ground. The voltage difference between the negative output voltage V_{OUT-} and the reference voltage V_{REF} is then converted into the phase delay using the delay chain (Fig. 4).

In Fig. 4, when V_{OUT-} is smaller than V_{REF}, the current sink of the upper delay chain decreases, and the upper delay chain shows the slow clock propagation. At the same time, the current source of the lower delay chain increases, and the lower delay chain shows fast clock propagation. As a result, the phase detector generates the logic low. In contrast, when V_{OUT-} is larger than V_{REF}, the current sink of the upper delay chain increases, and the clock propagation through the upper delay chain becomes faster. Also, the current source of the lower delay chain decreases, and the clock propagates more slowly through the lower delay chain. The phase detector then generates the logic high.

Then, the circuit enters the subtraction phase by turning Φ_1 on and Φ_2 off (Fig. 5 (c)). I_{REF}, which is set to be larger than I_{IN}, flows through C_F, and the integrated charge across C_F is subtracted. During the subtraction phase, the bias point of the OTA input is set to V_{CM} (= 500 mV). V_{OUT-} goes down, and the upper delay chain shows slow clock propagation.

In this way, the circuit repeats the integration and subtraction operations, and the phase detector generates a train of pulses at its output. The output pulse density is proportional to I_{IN}. The output pulses of PD_{OUT} are counted over the predetermined length (= 570 μs) of a sliding time window, and the corresponding digital output is generated.

This article has been accepted for publication in a future issue of this journal, but has not been fully edited. Content may change prior to final publication. Citation information: DOI 10.1109/ACCESS.2021.3107299, IEEE Access

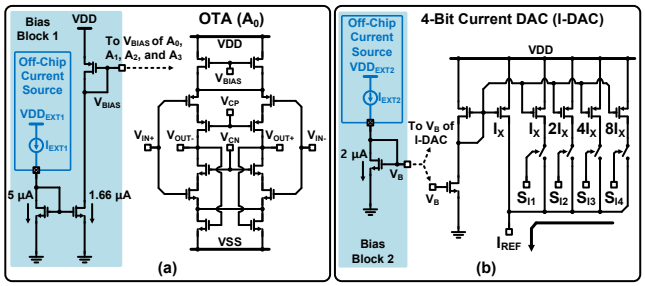

FIGURE 6. (a) Schematic of the self-biased cascode OTA used in the integrator. (b) 4-bit current DAC used in the fluorescence recording channel.

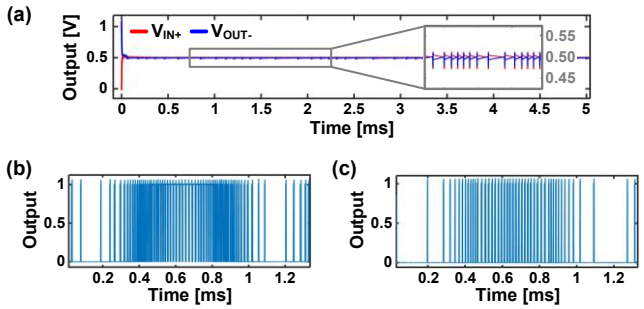

FIGURE 7. (a) Input and output voltage waveforms in the steady state. (b) Output bit stream when the switch S_{I1} in the current DAC is off, and (c) on.

To implement the integrator, a self-biased cascode OTA A_0 is used, as shown in Fig. 6 (a). A_0 is modified from the design in [12] by adding a cascode stage to improve the output impedance. To obtain a sufficiently low thermal noise level, it is designed to consume 600 nA. The sizes of the input transistors are set to 20 µm/0.25 µm for PMOS transistors and 10 µm/0.25 µm for NMOS transistors to mitigate the effect of 1/f noise. The bias current of A_0 is copied from the bias block 1. The bias voltage V_{BIAS} generated by this bias block 1 using an off-chip current source I_{EXT1} is shared by all the OTAs used in fluorescence and electrical recording channels. Also, the bias voltages, V_{CP} (= 300 mV) and V_{CN} (= 700 mV), are provided from the external supply. The input DC voltage V_{CM} of the A_0 is set to 500 mV, which is used as the reverse bias voltage to drive the photodiode. The measured dark current of the photodiode is smaller than 30 pA.

The magnitude of I_{REF} is controlled by a 4-bit (S_{I1}–S_{I4}) current DAC to accommodate a wider range of I_{IN} (Fig. 6 (b)). The I-DAC is driven by copying the bias current generated by the bias block 2 using an off-chip current source I_{EXT2}.

Fig. 7 (a) shows the input and output voltage waveforms in the steady state. Figs. 7 (b) and (c) show the operation examples of the current DAC. If I_{IN} is 10 nA and the switch S_{I1} in the current DAC is off, the output bit stream saturates (Fig. 7 (b)). To avoid this saturation, the magnitude of I_{REF} can be increased by turning on the switch S_{I1} (Fig. 7 (c)). In this way, the fluorescence recording channel accommodates I_{IN} ranging from 75 pA to 860 nA by controlling the switches (S_{I1}–S_{I4}) in the current DAC.

Note that the offset voltage caused by the input transistor mismatch in A_0 leads to the change in the baseline level of the recording circuit output. However, it does not affect the output amplitude, which is of our interest. We can control the I_{REF} generated by the I-DAC or the V_{REF} used in the delay chain to prevent the excessive baseline change from reducing the effective measurement range.

C. ELECTRICAL RECORDING CIRCUIT

Fig. 8 shows the electrical recording channels, which are composed of the CCIA-based analog front-ends (AFEs), SAR ADCs, and other circuit blocks. Thanks to the use of CCIA-based AFE, the DC electrode offset can be effectively suppressed. Each AFE consists of a low-noise amplifier (LNA), a variable gain amplifier (VGA), and an analog buffer. Two recording units, a digital multiplexer, and an output buffer are used to implement the 16-channel recording system (Fig. 8 (a)). Each recording unit consists of 8-channel AFEs, an analog multiplexer, and an ADC. In order to lower the power consumption while occupying the smaller silicon area, the 8-channel AFEs share an ADC through the 8-to-2 analog multiplexer. In particular, for reducing the power consumed by the analog buffer driving the input capacitor of SAR ADC, the sampling-time-extension technique is employed for the ADC [12]. Fig. 8 (b) presents the operation of the ADC with the timing diagram describing the sampling-time-extension technique.

The ADC is driven by two capacitive DACs. When the capacitive DAC 1 samples the current input signal V_{IN1}, the other capacitive DAC 2 quantizes the previously sampled signal V_{IN2}. The two DACs then switch their role when finishing the quantization of V_{IN2}. In this way, two DACs perform the sampling and quantization every 12 clocks, alternately. When carrying out the analog-to-digital conversion in the conventional manner, charging the input capacitive DAC for a limited sampling time while maintaining a sufficient sampling rate as well as accuracy increases the power consumption of the analog buffer significantly. To address this challenge, the sampling-time-extension technique effectively reduces the power consumption of the analog buffer, and the sampling rate and accuracy are maintained sufficiently high by alternately operating two capacitive DACs [12].

For *in vivo* use, the AFE and SAR ADC should be designed to have low noise characteristics and consume low power. The LNA is the most critical building block in the electrical recording channel for achieving low noise characteristics. To improve the current-noise efficiency, the inverter-based structure is used for the first stage A_1 (Fig. 9 (a)) [12], [13]. Compared to the structure based on a pair of PMOS (or NMOS) transistors for the input stage of the

This article has been accepted for publication in a future issue of this journal, but has not been fully edited. Content may change prior to final publication. Citation information: DOI 10.1109/ACCESS.2021.3107299, IEEE Access

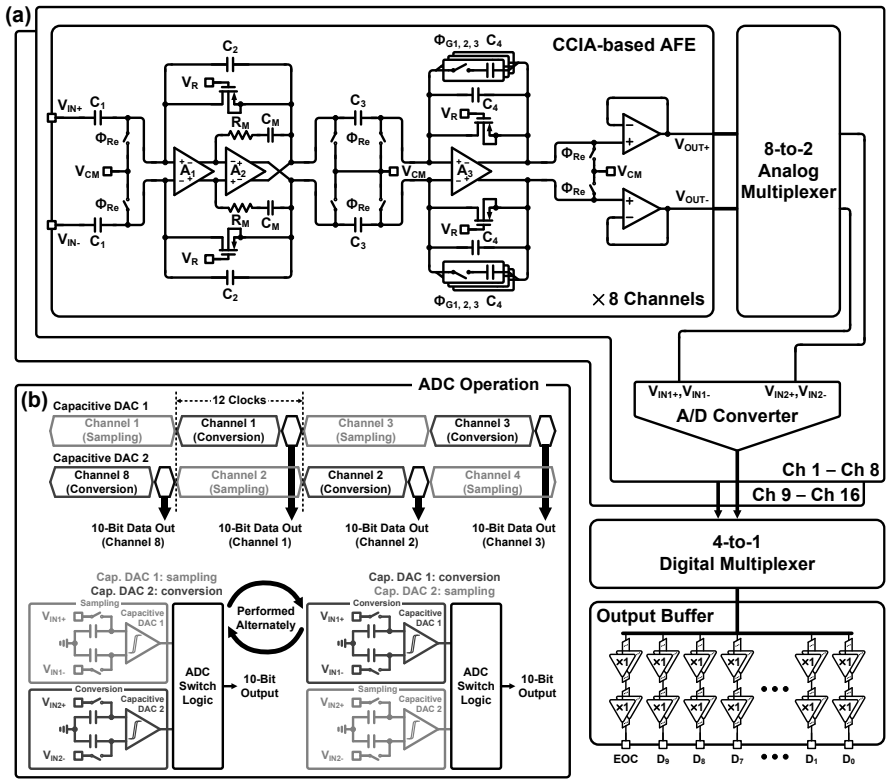

FIGURE 8. **(a) Block diagram of the CCIA-based electrical recording channels. (b) Operation of the analog-to-digital conversion.**

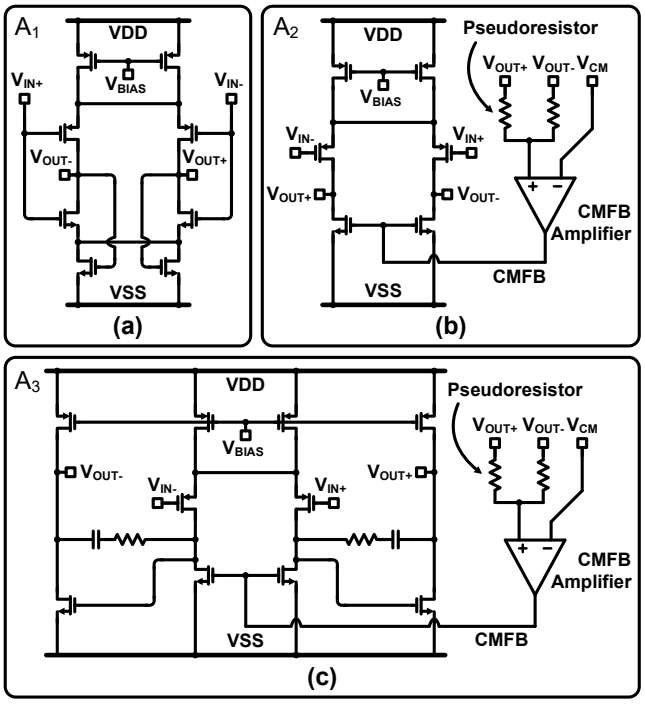

FIGURE 9. **(a) Schematic of the first stage A_1 used in the LNA. (b) Schematic of the second stage A_2 used in the LNA. (c) Schematic of the A_3 composing the VGA.**

LNA, the inverter-based structure provides doubled transconductance value while consuming the same current. Hence, it is possible to obtain improved input-referred noise characteristics. This input stage A_1 consumes 700 nA for thermal noise minimization. To suppress the 1/f noise effect, input transistors have large dimensions, such as 200 μm/1 μm for PMOS transistors and 300 μm/2 μm for NMOS transistors.

Then, to increase the LNA open-loop gain, the second stage A_2 follows the A_1 (Fig. 9 (b)). After the amplification of neural signals by the LNA, the VGA has to amplify the signals further to fit the optimal input range of the ADC so that the ADC's resolution performance can be fully utilized. The VGA requires relatively relaxed noise performance than the LNA, and thus the PMOS pair is used as the input stage of the VGA. Note that the effect of the input offset voltage of the LNA does not propagate to the following VGA because they are AC-coupled.

Fig. 9 (c) shows the widely used OTA structure, which is employed to implement A_3 composing the VGA. The output common-mode voltage of A_2 and A_3 is set to V_{CM} (= 500 mV) through the common-mode feedback (CMFB) loop consisting of two pseudoresistors and a CMFB amplifier. Similar to fluorescence recording channels, the bias current of A_1, A_2, and A_3 is copied from the bias block 1 shown in Fig. 6 (a) through V_{BIAS}.

Using the CCIA-based AFE has key advantages as follows: 1) It can be designed to have sufficient bandwidth while maintaining low power consumption, and 2) the DC electrode offset can be suppressed effectively. In the neural recording system, the AFE has to provide sufficiently low

This article has been accepted for publication in a future issue of this journal, but has not been fully edited. Content may change prior to final publication. Citation information: DOI 10.1109/ACCESS.2021.3107299, IEEE Access

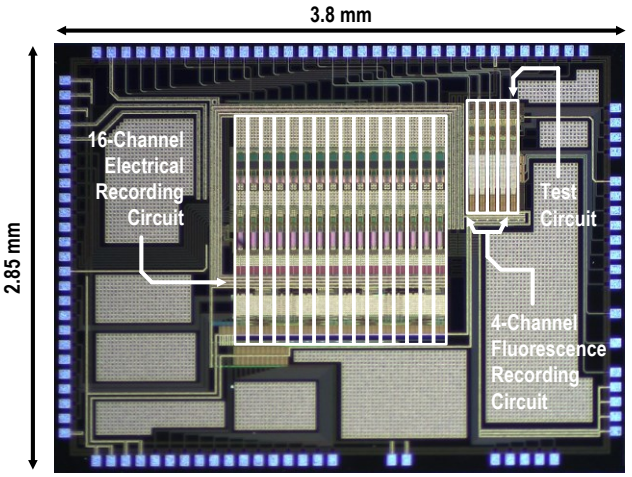

FIGURE 10. Die micrograph.

high-pass cutoff frequency (HPF) for monitoring LFP while removing the offset. In order to achieve such characteristics, the voltage-controlled PMOS pseudoresistor is used in the feedback path of the LNA and VGA (Fig. 8 (a)) [36], [37]. The gate voltage V_R is trimmed to have an HPF of sub-1 Hz.

IV. Chip Performances

Fig. 10 shows the die micrograph of the proposed multimodal neural activity readout IC fabricated using a 1-poly 6-metal (1P6M) 0.18-μm standard CMOS process. The IC occupies a total area of 3.8 mm × 2.85 mm. The active areas of the fluorescence recording channel and electrical recording channel are 0.05 mm^2 and 0.14 mm^2, respectively.

For testing the functionality of the fluorescence recording channel under the 1-V supply voltage, the multistep current is applied to the input of the fluorescence recording channel. Figs. 11 (a) and (b) show the output signals measured with varying the number of current steps from 4 to 32. The maximum current magnitude is maintained as 5 nA. The repetition frequency of the multistep current waveform is varied from 50 Hz to 6.25 Hz as the number of current steps changes from 4 to 32. In the top of Fig. 11 (a), the output bit stream is measured by applying the 4-step current input and reconstructed using the sliding time window. The reconstructed output bit stream shows a clear multistep current waveform, as shown in the bottom of Fig. 11 (a). The other reconstructed results also exhibit clear multistep waveforms, as shown in Fig. 11 (b). Fig. 11 (c) shows the output power spectral density when applying the DC input current of 300 nA, and the input-referred current noise is achieved as 22 pA_{RMS} over 500-Hz bandwidth.

To verify the detectable I_{IN} range of the fluorescence recording channel, the DC input current from 75 pA to 860 nA is applied while changing the magnitude of I_{REF} by

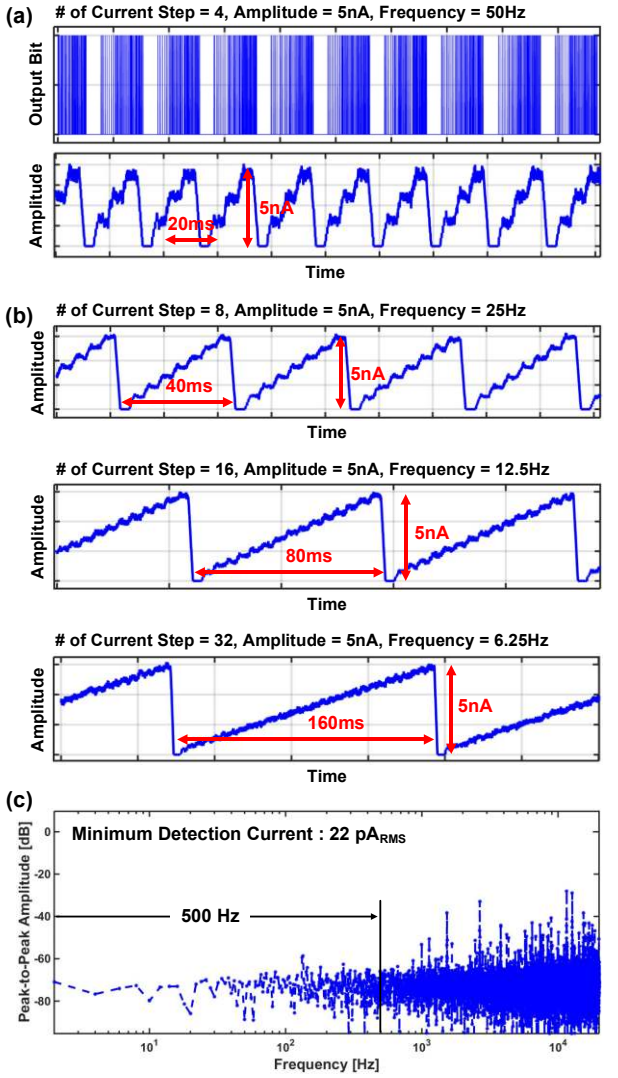

FIGURE 11. Measured AC characteristics of the fluorescence recording channel with the multistep current input having the amplitude of 5 nA: (a) 50-Hz input current with 4 steps; (b) 25-Hz input current with 8 steps, 12.5-Hz input current with 16 steps, and 6.25-Hz input current with 32 steps. (e) Power spectral density when applying the DC input current of 300 nA.

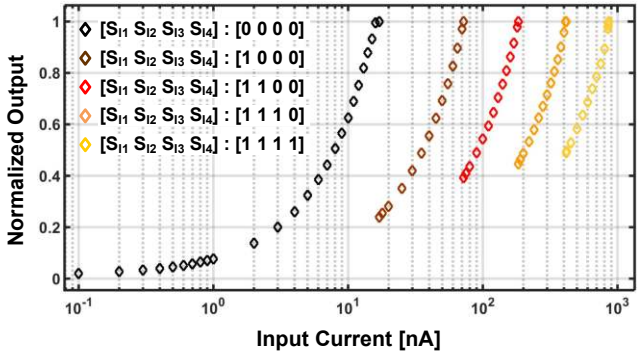

FIGURE 12. Measured DC characteristics of the fluorescence recording channel: all switches from S_{I1} to S_{I4} are turned on (yellow), S_{I4} is off (orange), S_{I3} and S_{I4} are off (red), S_{I2}–S_{I4} are off (brown), and S_{I1}–S_{I4} are off (black).

This article has been accepted for publication in a future issue of this journal, but has not been fully edited. Content may change prior to final publication. Citation information: DOI 10.1109/ACCESS.2021.3107299, IEEE Access

controlling the 4-bit I-DAC shown in Fig. 6 (b). The I-DAC increases the magnitude of I_{REF} by turning on the switches from S_{I1} to S_{I4}. By turning on each switch, the normalized output according to the DC input current is measured, as shown in Fig. 12. If the recording channel takes I_{IN} smaller than 17 nA, the I-DAC produces I_{REF} of I_X (= 124 nA). As I_{IN} increases up to 860 nA, the I-DAC produces I_{REF} of $16I_X$ (= 1.98 μA). The fluorescence recording channel consumes power from 724 nW/channel to 2.6 μW/channel as S_{I1}–S_{I4} are sequentially turned on. Each recording channel occupies an area of 0.05 mm^2/channel. Note that the power consumed by the bias blocks 1 and 2 shown in Fig. 6 is not counted in this channel power calculation. The power consumed by the bias blocks 1 and 2 is 10.66 μW and 3.6 μW, respectively. Since these bias blocks are shared by all the recording channels, the overall power consumption of the readout IC is not affected significantly.

Fig. 13 shows the measured gain-frequency response and the input-referred noise of the electrical recording channel. The system gain can be changed in the range from 61 dB to 73 dB (Fig. 13 (a)). The HPF is set by trimming V_R of the PMOS pseudoresistor shown in Fig. 8 (a). When V_R is set to 0.5 V, the HPF is measured to be about 15 Hz. The HPF can then be set to sub-1 Hz by increasing V_R up to 0.9 V. By setting the HPF to be sub-1 Hz, the LFPs can be well recorded without any signal loss, and the electrode offset can be filtered out effectively. The integrated input-referred noise is measured as 2.7 μV_{RMS} when it is integrated from 1 Hz to 10 kHz (Fig. 13 (b)). The spot noise density at 1 kHz is measured as 30 nV/√Hz. Fig. 13 (c) shows the time-domain measurement result of the input-referred noise. The peak-to-peak noise amplitude is measured as about 6 μV_{PP}. For testing the nonlinearity of the CCIA-based AFE, a single-tone test is performed using an input signal having an amplitude of 200 μV_{PP} at 1 kHz and 4 kHz (Figs. 14 (a) and (b)). The total harmonic distortion (THD) is measured as −35 dB at 1 kHz and −45 dB at 4 kHz. As shown in Fig. 13 (a), the low-pass cutoff frequency (LPF) is formed as 10 kHz, and thus the signal having a frequency higher than LPF is suppressed. Due to this filtering effect, the single-tone test with the input at 4 kHz shows an improved THD performance compared to the test with the input at 1 kHz.

Measured ADC performances are reported in Fig. 15. Fig. 15 (a) shows the ADC output code in the time domain measured when applying the rail-to-rail input voltage with a frequency of 1.013 kHz. The ADC is driven by the sampling rate of 200 kSamples/s and shared by 8-channel AFEs. The analog output of each AFE designed to have a 10-kHz bandwidth is converted to the digital code with the sampling rate of 25 kSamples/s. The output code of Fig. 15 (a) is processed to plot the power spectral density (PSD), as shown in Fig. 15 (b). The signal-to-noise-and-distortion ratio (SNDR) is achieved as 59.4 dB. The spurious-free dynamic range (SFDR) of 70 dB is obtained. The ADC is designed to have a 10-bit resolution, and the effective number of bits (ENOB) is measured as 9.6 bits after fabrication. The differential nonlinearity (DNL) spans from −0.38 LSB to +0.38 LSB, and the integral nonlinearity (INL) ranges from −0.34 LSB to +0.75 LSB (Fig. 15 (c)).

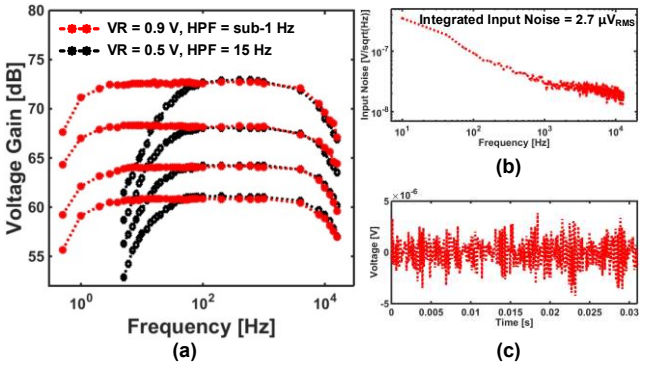

FIGURE 13. Measurement results of the electrical recording channel: (a) gain-frequency response, (b) input-referred noise in the frequency domain, and (c) input-referred noise in the time domain.

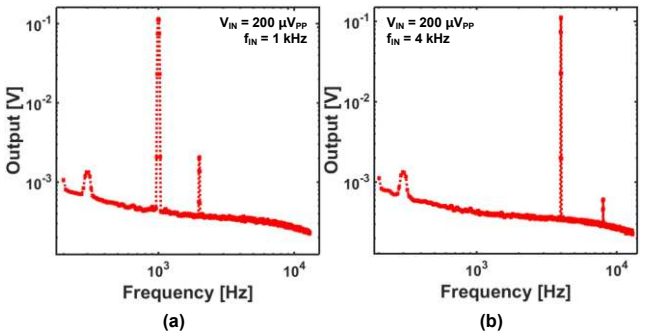

FIGURE 14. Measurement results of the single-tone test when applying the 200-μV_{PP} input voltage with the frequency of (a) 1 kHz and (b) 4 kHz.

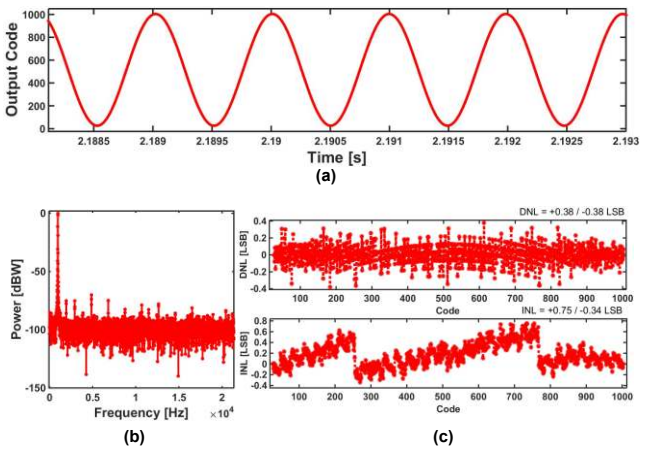

FIGURE 15. Measured performances of the 10-bit SAR ADC: (a) output code when applying the rail-to-rail input voltage with the frequency of 1 kHz, (b) power spectral density of the output code, and (c) differential nonlinearity ranging from –0.38 to +0.38 LSB and integral nonlinearity from –0.34 to +0.75 LSB.

This article has been accepted for publication in a future issue of this journal, but has not been fully edited. Content may change prior to final publication. Citation information: DOI 10.1109/ACCESS.2021.3107299, IEEE Access

The whole chain of the electrical recording channel consumes a power of 4.9 μW/channel under the 1-V supply voltage and occupies an area of 0.14 mm^2/channel. Note that the power consumed by the bias block 1 shown in Fig. 6 (a) is not included in the channel power calculation. Thanks to the inverter-based structure applied to the LNA, the implemented electrical recording channel achieves a noise-efficiency factor (NEF) of 2.3 and a power efficiency factor (PEF or NEF^2V_{DD}) of 5.29. The definitions of NEF and PEF are expressed in [38], [39].

V. Biological Measurement Results

The system functionality is verified through *in vitro* and *in vivo* experiments. Fig. 16 shows the experimental setup for measuring the Ca^{2+} concentration *in vitro* using the Oregon Green 488, which is used as the Ca^{2+} probe to mimic the GCaMP-based Ca^{2+} measurement. The Ca^{2+} probe emits fluorescent light when combined with Ca^{2+}. The optical fiber emits blue light to excite the Ca^{2+} probe. The fluorescent light emitted by the Ca^{2+} probe is detected through the photodiode. The photodiode is equipped with a filter that blocks the blue light so that the proportion of the photodiode current caused by the green fluorescence can be significantly enhanced. The photodiode current generated in response to the Ca^{2+} release is recorded through the fluorescence recording channel.

Fig. 17 (a) shows the close-up view of the photodiode and optical fiber inside the solution of the Oregon Green 488. As shown in Fig. 17 (a), two photodiodes are found. The photodiode in the solution generates the current by detecting the green fluorescence. The optical fiber placed to the left emits blue light, and the solution releases green fluorescence. In the outside of the solution, the blue light emitted from the optical fiber is seen. In this experiment, to build the environment as *in vivo* where the released Ca^{2+} concentration changes during the neural activation, Oregon Green 488 mixed with different Ca^{2+} concentrations is utilized, as shown in Fig. 17 (b). It is reported in [40] that the intracellular Ca^{2+} concentration is maintained lower than 0.1 μM in the resting state of the typical neurons and rises up to 10 μM under activation. Hence, solutions with the Ca^{2+} concentrations of 0 μM, 0.1 μM, 0.2 μM, 0.5 μM, 1 μM, 2 μM, 5 μM, 10 μM, and 20 μM are used for the test of the fluorescence recording channel (Fig. 17 (b)). Fig. 17 (c) presents the measured Ca^{2+} concentration through the photodiode and recording channel. The fluorescence change is expressed as $\Delta F/F$, which is defined as the ratio of the fluorescence intensity change ($F(t)$–$F_{Ca2+=0}$) to the nominal intensity for zero-Ca^{2+} condition ($F_{Ca2+=0}$). Fig. 17 (d) shows the photodiode current measured with changing the white light intensity emitted to the photodiode. The functionality of the electrical recording channel is verified using the pre-recorded neural spike data. The pre-recorded

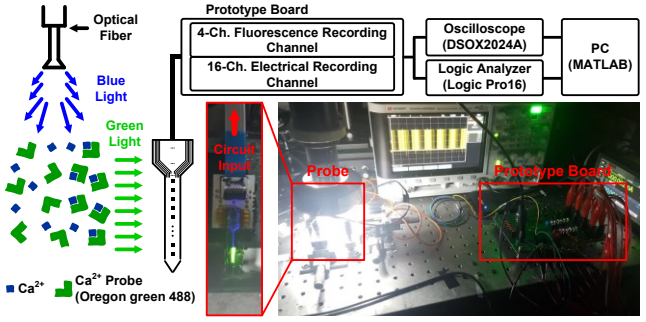

FIGURE 16. Experimental setup using Oregon Green 488 to mimic the GCaMP-based Ca^{2+} measurement.

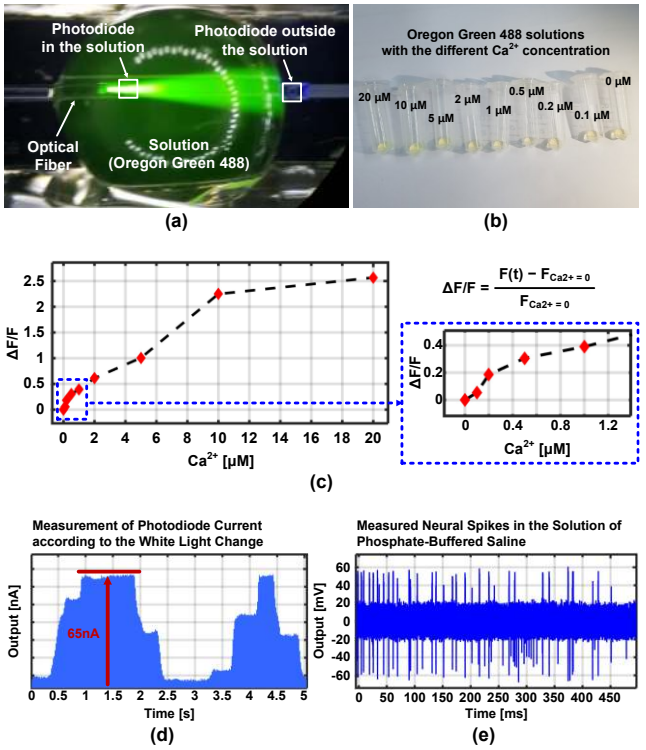

FIGURE 17. (a) Fluorescent light measurement setup using the photodiode, optical fiber, and Oregon Green 488. (b) Solutions (Oregon Green 488) with different Ca^{2+} concentrations. (c) Measured Ca^{2+} concentration through the photodiode and fluorescence recording channel. (d) Photodiode current measured with changing the intensity of the white light emitted to the photodiode. (e) Measured neural spikes in the phosphate-buffered saline through the electrical recording channel.

data are reproduced using the LabVIEW DAC and applied to the phosphate-buffered saline (PBS). Fig. 17 (e) shows neural spikes successfully measured using the electrical recording channel in the PBS.

After the completion of the *in vitro* experiment using the multimodal neural activity readout IC, the *in vivo* experiment is carried out using the mouse model. In this experiment, to measure the fluorescent light change according to the neural activity, the Ca^{2+} probe is injected into a mouse brain. 4 weeks after the Ca^{2+} probe injection, the photodiode is inserted into the region of hippocampus

This article has been accepted for publication in a future issue of this journal, but has not been fully edited. Content may change prior to final publication. Citation information: DOI 10.1109/ACCESS.2021.3107299, IEEE Access

CA1. The insertion point is 1.71 mm to the right of the bregma and 2 mm to the bottom of the bregma. The measurement is performed by changing the insertion depth from 1.57 mm to 1.7 mm. Fig. 18 (a) shows the photodiode insertion point and the sagittal plane of a mouse brain for describing the measurement of the fluorescent light from the region of hippocampus CA1. After inserting the photodiode, the optical fiber mounted on the photodiode excites the Ca^{2+} probe by emitting blue light, as shown in Fig. 18 (b). The mouse used in the experiment is C57BL/6J. GCaMP6f is used as the Ca^{2+} probe. This probe is specifically combined with the excitatory neurons in the CA1 region of the mouse brain. The GCaMP6f is excited with the blue light, which has an intensity of 4.8×10^{-2} mW/cm^2. To determine the baseline current of the photodiode during the fluorescence recording, the photodiode current is measured by turning on and off the blue light (Fig. 18 (c)). The photodiode current of 45 nA is measured when the blue light is turned on to induce the fluorescent light, while the photodiode current is nearly zero when the blue light is turned off. All *in vitro* and *in vivo* related experimental procedures were approved by the Korea Institute of Science and Technology (KIST) and carried out in accordance with the ethical standards stated in the Animal Care and Use Guidelines of the KIST.

The measured fluorescence intensity change using GCaMP6f is presented in Fig. 18 (d). The signal shows the fluorescence change from 0.6 % to 1.4 % and has a duration of several hundreds of ms. Converting the measured fluorescence change into the current value, the current varies from 270 pA to 630 pA. Fig. 18 (e) shows the measured neural spikes using the electrical recording channel in the mouse brain. The spike amplitude is distributed from 40 μV_{PP} to 100 μV_{PP} with a duration of 2.5 ms.

Table I presents a summary of the measured performances and a comparison with the prior works. Compared with the prior works, the proposed IC can measure the Ca^{2+} concentration along with the electrical signals, and thus the cell-type-specific neural recording can be carried out.

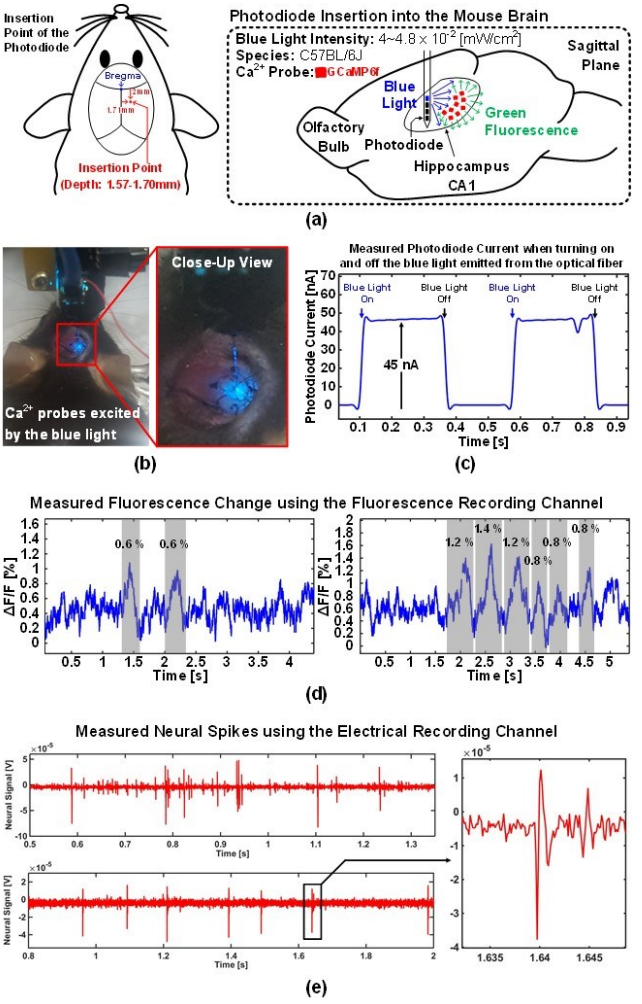

FIGURE 18. (a) Photodiode insertion point and diagram for G-CaMP-based *in vivo* experiment using a mouse model of C57BL/6J. (b) Top view of *in vivo* experiment when inserting the photodiode to the hippocampus and emitted blue light through the optical fiber. (c) Measured photodiode current when turning on and off the blue light. (d) Measured fluorescence change using the fluorescence recording channel 4 weeks after injection of the GCaMP6f. (e) Measured neural spikes using the electrical recording channel.

VI. Conclusion

In this paper, we report a multimodal neural activity readout IC that can perform a cell-type-specific study of a heterogeneous cell population by monitoring the Ca^{2+} concentration along with the electrical signals. To implement an energy-efficient system, a time-based topology is applied to the fluorescence recording channel, and an instrumentation-amplifier-based topology is employed for the electrical recording channel. The prototype IC is implemented in a 1P6M 0.18-μm standard CMOS process. 724 nW/channel of power is consumed for fluorescence recording while achieving a recording range from 75 pA to 860 nA. 4.9 μW/channel of power is consumed for electrical recording. The implemented IC successfully demonstrates the measurement of the Ca^{2+} concentration and electrical signals while providing the required performance for both fluorescence and electrical recording functions.

REFERENCES

[1] C. M. Lopez, D. Prodanov, D. Braeken, I. Gligorijevic, W. Eberle, C. Bartic, R. Puers, and G. Gielen, "A multichannel integrated circuit for electrical recording of neural activity, with independent channel programmability," *IEEE Transactions on Biomedical Circuits and Systems*, vol. 6, no. 2, pp. 101–110, Apr. 2012.

This article has been accepted for publication in a future issue of this journal, but has not been fully edited. Content may change prior to final publication. Citation information: DOI 10.1109/ACCESS.2021.3107299, IEEE Access

TABLE I
PERFORMANCE SUMMARY AND COMPARISON WITH THE PRIOR WORKS

	JSSC [4]	JSSC [6]	TCAS- I [12]	JSSC [14]	This Work
Year	2018	2017	2013	2009	
Process	0.13-μm	0.18-μm	0.18-μm	0.5-μm	0.18-μm
Supply	1.2-V, 1.8-V, 3.3-V	--	1-V, 1.8-V	2.5-V	1-V (Core), 1.8-V (I/O)
Sensing Type	AP / LFP / IM	Dopamine / AP / LFP / IM	AP / LFP	Dopamine / AP / LFP	Ca^{2+} / AP / LFP
Dark Current	--	--	--	--	< 30 pA
Detection Range	--	--	--	--	81 dB (75 pA - 860 nA)
Input-Referred Noise	7.5 μV_{rms} (AP Band) 12 μV_{rms} (Full Band)	5.4 μV_{rms}	4 μV_{rms}	3.5 μV_{rms}	2.7 μV_{rms}
NEF	--	--	1.9	--	2.3
PEF (= NEF^2V_{DD})	--	--	3.6	--	5.29
Gain	6 - 69 dB	29 - 77 dB	54.8 / 60.9 dB	Direct Conversion	61 - 73 dB
Bandwidth	0.5 Hz - 10 kHz	1 Hz - 10 kHz	0.38 Hz - 5.1 kHz	1.1 Hz - 5 kHz	1 Hz - 10 kHz
Resolution	10 bit	10 bit	9 bit	--	10 bit
ENOB	--	--	8.3 bit	--	9.6 bit
DNL	--	--	±0.55	--	+0.38/–0.38 LSB
INL	--	--	±1.2	--	+0.75/–0.35 LSB
SNDR	--	56.2 dB	51.5 dB	--	59.4 dB
SFDR	--	--	--	--	70dB
Power	[A,B] 45.8 μW (ER)	[D] 86 mW	[A,B] 4.5 μW (ER)	[B] 76 μW (CR) [B] 86 μW (ER)	[B] 724 nW (FR) [B] 4.9 μW (ER)
Area	[E] 192 mm^2	[E] 106.8 mm^2	[E] 28.2 mm^2	[A,C] 0.16 mm^2 (CR/ ER)	[C] 0.05 mm^2 (FR) [C] 0.14 mm^2 (ER)

[A] Calculated based on the published paper, [B] Power per channel, [C] Area per channel, [D] Total power, [E] Total area
ER : electrical recording, FR : fluorescence recording, CR : chemical recording

[2] C. M. Lopez, A. Andrei, S. Mitra, M. Welkenhuysen, W. Eberle, C. Bartic, R. Puers, R. F. Yazicioglu, and G. G. E. Gielen, "An implantable 455-active-electrode 52-channel CMOS neural probe," *IEEE Journal of Solid-State Circuits*, vol. 49, no. 1, pp. 248–261, Jan. 2014.

[3] C. M. Lopez, J. Putzeys, B. C. Raducanu, M. Ballini, S. Wang, A. Andrei, V. Rochus, R. Vandebriel, S. Severi, C. V. Hoof, S. Musa, N. V. Helleputte, R. F. Yazicioglu, and S. Mitra, "A neural probe with up to 966 electrodes and up to 384 configurable channels in 0.13 μm SOI CMOS," *IEEE Transactions on Biomedical Circuits and Systems*, vol 11, no. 3, pp. 510–522, Jun. 2017.

[4] C. M. Lopez, H. S. Chun, S. Wang, L. Berti, J. Putzeys, C. V. D. Bulcke, J.-W. Weijers, A. Firrincieli, V. Reumers, D. Braeken, and N. V. Helleputte, "A multimodal CMOS MEA for high-throughput intracellular action potential measurements and impedance spectroscopy in drug-screening applications," *IEEE Journal of Solid-State Circuits*, vol. 53, no. 11, pp. 3076–3086, Nov. 2018.

[5] M. Ballini, J. Muller, P. Livi, Y. Chen, U. Frey, A. Stettler, A. Shadmani, V. Viswam, I. L. Jones, D. Jackel, M. Radivojevic, M. K. Lewandowska, W. Gong, M. Fiscella, D. J. Bakkum, F. Heer, and A. Hierlemann, "A 1024-channel CMOS microelectrode array with 26,400 electrodes for recording and stimulation of electrogenic cells in vitro," *IEEE Journal of Solid-State Circuits*, vol. 49, no. 11, pp. 2705–2719, Nov. 2014.

[6] J. Dragas, V. Viswam, A. Shadmani, Y. Chen, R. Bounik, A. Stettler, M. Radivojevic, S. Geissler, M. E. J. Obien, J. Muller, and A. Hierlemann, "*In vitro* multi-functional microelectrode array featuring 59760 electrodes, 2048 electrophysiology channels, stimulation, impedance measurement, and neurotransmitter detection channels," *IEEE Journal of Solid-State Circuits*, vol. 52, no. 6, pp. 1576–1590, Jun. 2017.

[7] B. C. Johnson, S. Gambini, I. Izyumin, A. Moin, A. Zhou, G. Alexandrov, S. R. Santacruz, J. M. Rabaey, J. M. Carmena, and R. Muller, "An implantable 700μW 64-channel neuromodulation IC for simultaneous recording and stimulation with rapid artifact recovery," *IEEE Symposium on VLSI Circuits (SOVC) Dig. Tech. Papers*, Jun. 2017, C48–C49.

[8] M. Ballini, J. Bae, N. Marrocco, R. Verplancke, D. Schaubroeck, D. Cuypers, M. Cauwe, J. O'Callaghan, A. Fahmy, N. Maghari, R. Bashirullah, C. V. Hoof, N. V. Helleputte, M. O. D. Beeck, D. Braeken, and S. Mitra, "Intraneural active probe for bidirectional peripheral nerve interface," *IEEE Symposium on VLSI Circuits (SOVC) Dig. Tech. Papers*, Jun. 2017, C50–C51.

[9] T. Chi, J. S. Park, J. C. Butts, T. A. Hookway, A. Su, C. Zhu, M. P. Styczynski, T. C. McDevitt, and H. Wang, "A multi-modality CMOS sensor array for cell-based assay and drug screening," *IEEE Transactions on Biomedical Circuits and Systems*, vol. 9, no. 6, pp. 801–814, Dec. 2015.

[10] J. S. Park, T. Chi, A. Su, C. Zhu, J. H. Sung, H. C. Cho, M. Styczynski, and H. Wang, "A high-density CMOS multi-modality joint sensor/stimulator array with 1024 pixels for holistic real-time cellular characterization," *IEEE Symposium on VLSI Circuits (SOVC) Dig. Tech. Papers*, Jun. 2016, pp. 1–2.

[11] J. Park, M. K. Aziz, S. Gonzalez, D. Jung, T. Chi, S. Li, H. C. Cho, and H. Wang, "A CMOS 22k-pixel single-cell resolution multi-modality real-time cellular sensing array," *IEEE Custom Integrated Circuits Conference (CICC) Dig. Tech. Papers*, Apr. 2017, pp. 1–4.

[12] X. Zou, L. Liu, J. H. Cheong, L. Yao, P. Li, M.-Y. Cheng, W. L. Goh, R. Rajkumar, G. S. Dawe, K.-W. Cheng, and M. Je, "A 100-channel 1-mW implantable neural recording IC," *IEEE Transactions on Circuits and Systems–I: Regular Papers*, vol. 60, no. 10, pp. 2584–2596, Oct. 2013.

[13] D. Han, Y. Zheng, R. Rajkumar, G. S. Dawe, and M. Je, "A 0.45 V 100-channel neural-recording IC with sub-μW/channel consumption in 0.18 μm CMOS," *IEEE Transactions on Biomedical Circuits and Systems*, vol. 7, no. 6, pp. 735–746, Dec. 2013.

[14] M. Roham, D. P. Covey, D. P. Daberkow, E. S. Ramsson, C. D. Howard, B. A. Heidenreich, P. A. Garris, and P. Mohseni, "A wireless IC for time-share chemical and electrical neural recording," *IEEE Journal of Solid-State Circuits*, vol. 44, no. 12, pp. 3645–3658, Dec. 2009.

[15] B. Bozorgzadeh, D. Schuweiler, M. Bobak, P. A. Garris, and P. Mohseni, "Neurochemical thermostat: a neural interface SoC with integrated chemometrics for closed-loop regulation of brain dopamine," *IEEE Symposium on VLSI Circuits (SOVC) Dig. Tech. Papers*, Jun. 2015, C110–C111.

[16] T. Lee, J.-H. Park, J.-H Cha, N. Chou, D. Jang, J.-H. Kim, I.-J. Cho, S.-J Kim, and M. Je, "A multimodal multichannel neural activity readout IC with 0.7μW/channel Ca^{2+}-probe-based fluorescence recording and electrical recording," *IEEE Symposium on VLSI Circuits (SOVC) Dig. Tech. Papers*, Jun. 2019, C290–C291.

[17] J. Nakai, M. Ohkura, and K. Imoto, "A high signal-to-noise Ca^{2+} probe composed of a single green fluorescent protein," *Nature Biotechnology*, vol. 19, pp. 137–141, Feb. 2001.

[18] J. Akerboom *et al*., "Genetically encoded calcium indicator for multi-color neural activity imaging and combination with optogenetics," *Frontiers in Molecular Neuroscience*, vol. 6, pp. 1–29, Mar. 2013.

[19] K. Najafi and K. D. Wise, "An implantable multielectrode array with on-chip signal processing," *IEEE Journal of Solid-State Circuits*, vol. SC-21, no. 6, pp. 1035–1044, Dec. 1986.

[20] R. R. Harrison and C. Charles, "A low-power low-noise CMOS amplifier for neural recording applications," *IEEE Journal of Solid-State Circuits*, vol. 38, no. 6, pp. 958–965, Jun. 2003.

[21] C. Stosiek, O. Garaschuk, K. Holthoff, and A. Konnerth, "In vivo two-photon calcium imaging of neuronal networks," *Proceedings of the National Academy of Science of the U. S. A*, vol. 100, no. 12, pp. 7319–7324, Jun. 2003.

[22] G. Ji, M. E. Feldman, K.-Y. Deng, K. S. Greene, J. Wilson, J. C. Lee, R. C. Johnston, M. Rishniw, Y. Tallini, J. Zhang, W. G. Wier, M. P. Blaustein, H.-B. Xin, J. Nakai, and M. I. Kotlikoff, "Ca^{2+}-sensing transgenic mice," *The Journal of Biological Chemistry*, vol. 279, no. 20, pp. 21461–21468, May 2014.

[23] Y. LeChasseur, S. Dufour, G. Lavertu, C. Bories, M. Deschenes, R. Vallee, and Y. D. Koninck, "A microprobe for parallel optical and electrical recordings from single neurons *in vivo*," *Nature Methods*, vol. 8, no. 4, pp. 319–325, Apr. 2011.

[24] Y. Gong, C. Huang, J. Z. Li, B. F. Grewe, Y. Zhang, S. Eismann, and M. J. Schnitzer, "High-speed recording of neural spikes in awake mice and flies with a fluorescent voltage sensor," *Science*, vol. 350, no. 6266, pp. 1361–1366, Dec. 2015.

[25] D. Camillo, M. Ahmadlou, M. H. Saiepour, M. Yasaminshirazi, C. N. Levelt, and J. A. Heimel, "Visual processing by calretinin expressing inhibitory neurons in mouse primary visual cortex," *Scientific Reports*, vol.8, no. 12355, pp. 1–13, Aug. 2018.

[26] H. Chandrakumar and D. Markovic, "A high dynamic-range neural recording chopper amplifier for simultaneous neural recording and stimulation," *IEEE Journal of Solid-State Circuits*, vol. 52, no. 3, pp. 645–656, Mar. 2017.

[27] H. Chandrakumar and D. Markovic, "An 80-mV_{pp} linear-input range, 1.6-GΩ input impedance, low-power chopper amplifier for closed-loop neural recording that is tolerant to 650-mV_{pp} common-mode interference," *IEEE Journal of Solid-State Circuits*, vol. 52, no. 11, pp. 2811–2828, Nov. 2017.

[28] H. Chandrakumar and D. Markovic, "A 15.2-ENOB 5-kHz BW 4.5-μW chopped CT $\Delta\sum$-ADC for artifact-tolerant neural recording front ends," *IEEE Journal of Solid-State Circuits*, vol. 53, no. 12, pp. 3470–3483, Dec. 2018.

[29] A. Benazzouz, O. Mamad, P. Abedi, R. Bouali-Benazzouz, and J. Chetrit, "Involvement of dopamine loss in extrastriatal basal ganglia nuclei in the pathophysiology of Parkinson's disease," *Frontiers in Aging Neuroscience*, vol. 6, no. 87, pp. 1–5, May 2014.

[30] M. Berger, J. A. Gray, and B. L. Roth, "The expanded biology of serotonin," *Annual Review of Medicine*, pp. 355–366, 2009.

[31] V. Viswam, R. Bounik, A. Shadmani, J. Dragas, C. Urwyler, J. A. Boos, M. E. J. Obien, J. Muller, Y. Chen, and A. Hierlemann, "Impedance spectroscopy and electrophysiological imaging of cells with a high-density CMOS microelectrode array system," *IEEE Transactions on Biomedical Circuits and Systems*, vol. 12, no. 6, pp. 1356–1368, Dec. 2018.

[32] Y. Pan, D. Jiang, C. Gu, Y. Qiu, H. Wan, and P. Wang, "3D microgroove electrical impedance sensing to examine 3D cell cultures for antineoplastic drug assessment," *Microsystems & Nanoengineering*, vol. 6, no. 23, pp. 1–10, Mar. 2020.

[33] F. Asphahani and M. Zhang, "Cellular impedance biosensors for drug screening and toxin detection," *Analyst*, vol. 132, no. 9, pp. 835–841, Sep. 2007.

[34] Y. Chen, C. C. Wong, T. S. Pui, R. Nadipalli, R. Weerasekera, J. Chandran, H. Yu, and A. R. A. Rahman, "CMOS high density electrical impedance biosensor array for tumor cell

detection," *Sensors and Actuators B: Chemical*, vol. 173, pp. 903–907, Oct. 2012.

[35] S.-K Lee, S.-J. Park, H.-J. Park, and J.-Y. Sim, "A 21fJ/conversion-step 100 kS/s 10-bit ADC with a low-noise time-domain comparator for low-power sensor interface," *IEEE Journal of Solid-State Circuits*, vol. 46, no. 3, pp. 651–659, Mar. 2011.

[36] S. Ha, C. Kim, Y. M. Chi, A. Akinin, C. Maier, A. Ueno, and G. Cauwenberghs, "Integrated circuits and electrode interfaces for noninvasive physiological monitoring," *IEEE Transactions on Biomedical Circuits and Systems*, vol. 61, no. 5, pp. 1522–1537, May 2014.

[37] T. Lee, S. Hong, C. Jung, J. Lee, and M. Je, "A 1-V 4.6-μW/channel fully differential neural recording front-end IC with current-controlled pseudoresistor in 0.18-μm CMOS," *Journal of Semiconductor Technology and Science*, vol. 19, no. 1, pp. 30–41, Feb. 2019.

[38] M. S. J. Steyaert, W. M. C. Sansen, and C. Zhongyuan, "A micropower low-noise monolithic instrumentation amplifier for medical purposes," *IEEE Journal of Solid-State Circuits*, vol. SC-22, no. 6, pp. 1163–1168, Dec. 1987.

[39] R. Muller, S. Gambini, and J. M. Rabaey, "A 0.013 mm^2, 5 μW, DC-coupled neural signal acquisition IC with 0.5 V supply," *IEEE Journal of Solid-State Circuits*, vol. 47, no. 1, pp. 232–243, Jan. 2012.

[40] L. Lu, P. Gutruf, L. Xia, D. L. Bhatti, X. Wang, A. Vazquez-Guardado, X. Ning, X. Shen, T. Sang, R. Ma, G. Pakeltis, G. Sobczak, H. Zhang, D.-O, Seo, M. Xue, L. Yin, D. Chanda, X. Sheng, M. R. Bruchas, and J. A. Rogers, "Wireless optoelectronic photometers for monitoring neuronal dynamics in the deep brain," *Proceedings of the National Academy of Science of the U. S. A*, vol. 115, no. 7, pp. 1374–1383, Jan. 2018.

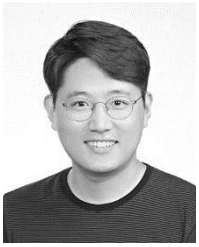

Taeju Lee received the B.S. degree in electrical, electronics and communication engineering from the Korea University of Technology and Education (KOREATECH), Cheonan, South Korea, in 2014, the M.S. degree in information and communication engineering from the Daegu Gyeongbuk Institute of Science and Technology (DGIST), Daegu, South Korea, in 2016, and the Ph.D. degree in electrical engineering from the Korea Advanced Institute of Science and Technology (KAIST), Daejeon, South Korea, in 2021.

From 2014 to 2016, he was with the DGIST, where he was involved in developing neural recording ICs and brain rehabilitation systems. From 2017 to 2020, he was with the KAIST, where he developed multichannel electrical neural recording ICs and led the development of multimodal neural recording ICs monitoring APs/LFPs/Calcium ions for conducting the cell-type-specific study in complex neural networks. He is currently a Postdoctoral Researcher at the IMPACT Lab, KAIST. His current research interests include neural interfaces focusing on the monitoring of multiple neural signals.

Jee-Ho Park (S'17) received his B.S. degree in electrical engineering from the Ulsan National Institute of Science and Technology (UNIST), Ulsan, South Korea, in 2018 where he is currently pursuing the M.S./Ph.D. degree.

His current research interests include Fast start-up Oscillator, VCO-based ADC and CMOS-based biomedical interface circuits and systems.

Namsun Chou received the B.S. in Mechanical engineering from Konkuk University, Seoul, Korea, in 2009, and M.S. and Ph.D. degrees in Mechatronics from Gwangju Institute of Science and Technology (GIST), Gwangju, Korea, in 2011 and 2016, respectively.

From 2016 to 2017, he worked in the Department of Robotics Engineering, Daegu Gyeongbuk Institute of Science and Technology (DGIST), Daegu, Korea as a Postdoctoral Fellow. He is currently Postdoctoral Fellow at the Center for BioMicrosystems, Brain Science Institute, Korea Institute of Science and Technology (KIST), Seoul, Korea.

His current research interests include MEMS neural probe system for recording neural activity with various stimulation, miniaturized fluorescence detection system in vivo, and miniaturized ultrasound stimulation system for neuromodulation.

Il-Joo Cho received the B.S., M.S., and Ph.D. degrees in electrical engineering from the Korea Advanced Institute of Science and Technology (KAIST), Daejeon, South Korea, in 1998, 2000, and 2004, respectively.

From 2004 to 2007, he worked at the LG Electronics Institute of Technology, Seoul, as a Senior Research Scientist. From 2007 to 2008, he worked with the Electrical Engineering and Computer Science (EECS) Department, University of Minnesota, Minneapolis, MN, USA, as a Research Fellow. From 2008 to 2010, he worked with the Electrical Engineering and Computer Science University of Michigan, Ann Arbor, MI, USA, as a Visiting Research Scientist. In 2010, he joined the Center for BioMicrosystems, Brain Science Institute, Korea Institute of Science and Technology (KIST), Seoul, where he is currently the Head of the Center for BioMicrosystems.

This article has been accepted for publication in a future issue of this journal, but has not been fully edited. Content may change prior to final publication. Citation information: DOI 10.1109/ACCESS.2021.3107299, IEEE Access

Seong-Jin Kim (S'04–M'10) received his B.S. degree in electrical engineering from the Pohang University of Science and Technology, Pohang, South Korea, in 2001, and M.S. and Ph.D. degrees in electrical engineering from KAIST, Daejeon, South Korea, in 2003 and 2008, respectively.

From 2008 to 2012, he was a Research Staff Member at the Samsung Advanced Institute of Technology, Yongin, South Korea, where he was involved in the development of CMOS imager for real-time acquisition of 3-D images. From 2012 to 2015, he was with the Institute of Microelectronics, A*STAR, Singapore, where he was involved in the design of analog-mixed signal circuits for various sensing systems. In 2015, he joined the School of Electrical and Computer Engineering, Ulsan National Institute of Science and Technology, Ulsan, South Korea as an Assistant Professor. His current research interests include high performance imaging devices, and biomedical interface circuits and systems.

Minkyu Je (S'97-M'03-SM'12) received the M.S. and Ph.D. degrees, both in Electrical Engineering and Computer Science, from Korea Advanced Institute of Science and Technology (KAIST), Daejeon, Korea, in 1998 and 2003, respectively. In 2003, he joined Samsung Electronics, Giheung, Korea, as a Senior Engineer and worked on multi-mode multi-band RF transceiver SoCs for GSM / GPRS / EDGE / WCDMA standards. From 2006 to 2013, he was with Institute of Microelectronics (IME), Agency for Science, Technology and Research (A*STAR), Singapore. He worked as a Senior Research Engineer from 2006 to 2007, a Member of Technical Staff from 2008 to 2011, a Senior Scientist in 2012, and a Deputy Director in 2013. From 2011 to 2013, he led the Integrated Circuits and Systems Laboratory at IME as a Department Head. In IME, he led various projects developing low-power 3D accelerometer ASICs for high-end medical motion sensing applications, readout ASICs for nanowire biosensor arrays detecting DNA/RNA and protein biomarkers for point-of-care diagnostics, ultra-low-power sensor node SoCs for continuous real-time wireless health monitoring, and wireless implantable sensor ASICs for medical devices, as well as low-power radio SoCs and MEMS interface/control SoCs for consumer electronics and industrial applications. He was also a Program Director of NeuroDevices Program under A*STAR Science and Engineering Research Council (SERC) from 2011 to 2013, and an Adjunct Assistant Professor in the Department of Electrical and Computer Engineering at National University of Singapore (NUS) from 2010 to 2013. He was an Associate Professor in the Department of Information and Communication Engineering at Daegu Gyeongbuk Institute of Science and Technology (DGIST), Korea from 2014 to 2015. Since 2016, he has been an Associate Professor in the School of Electrical Engineering at Korea Advanced Institute of Science and Technology (KAIST), Korea.

His main research areas are advanced IC platform development including smart sensor interface ICs and ultra-low-power wireless communication ICs, as well as microsystem integration leveraging the advanced IC platform for emerging applications such as intelligent miniature biomedical devices, ubiquitous wireless sensor nodes, and future mobile devices. He is an author of 5 book chapters, and has more than 260 peer-reviewed international conference and journal publications in the areas of sensor interface IC, wireless IC, biomedical microsystem, 3D IC, device modeling and nanoelectronics. He also has more than 40 patents issued or filed. He has served on the Technical Program Committee and Organizing Committee for various international conferences, symposiums and workshops including IEEE International Solid-State Circuits Conference (ISSCC), IEEE Asian Solid-State Circuits Conference (A-SSCC) and IEEE Symposium on VLSI Circuits (SOVC).